

Supporting Information for

Topologically Immobilized Catalysis Centre for Long-term Stable Carbon Dioxide Reforming of Methane

Shusaku Shoji, Xiaobo Peng,* Tsubasa Imai, Paskalis Sahaya Murphin Kumar, Kimitaka Higuchi, Yuta Yamamoto, Tomoharu Tokunaga, Shigeo Arai, Shigenori Ueda, Ayako Hashimoto, Noritatsu Tsubaki, Masahiro Miyauchi, Takeshi Fujita,* and Hideki Abe*

Contents

Experimental details

Figure S1: Low-temperature DRM over the Ni#Y₂O₃ catalyst at different temperatures.

Figure S2: SEM images of NiY (NiY = 1:1) alloy particles.

Figure S3: Formation mechanism of the rooted structure of Ni#Y₂O₃.

Figure S4: *p*XRD patterns for the alloy precursors.

Figure S5: SEM images of the Ni-Y₂O₃ nanocomposites obtained from different Ni-Y alloy precursors.

Figure S6: STEM images of the Ni#Y₂O₃ catalyst.

Figure S7: Another Ni-Y₂O₃ composite obtained by different atmospheric processing.

Figure S8: The lattice fringes for Ni#Y₂O₃ catalyst.

Figure S9: Influence of the Y content on H₂ chemisorption and Ni dispersion.

Figure S10: TEM observation and Ni particle size distribution for Ni#Y₂O₃, Ni/Al₂O₃, Ni/Y₂O₃.

Figure S11: Stability of the Ni#Y₂O₃ in LT-DRM in a dense gas condition.

Figure S12: *p*XRD patterns for the NiY alloy, fresh Ni#Y₂O₃ and Ni#Y₂O₃ after use.

Figure S13: SEM image of a used Ni/Al₂O₃ catalyst.

Figure S14: Compositional mapping images for the Ni#Y₂O₃ catalyst after use.

Figure S15: Raman spectra for Ni/Al₂O₃, Ni/Y₂O₃ and Ni#Y₂O₃ after use.

Figure S16: Hard X-ray photoemission spectra (HAXPES) in Ni2*p*- and C1*s* regions for the catalysts after use.

Figure S17: Thermo-gravimetry (TG) and differential temperature analysis (TDA) results for Ni#Y₂O₃, Ni/Y₂O₃ and Ni/Al₂O₃.

Figure S18: Conventional TEM- and *in-situ* TEM images for Ni/Y₂O₃.

Figure S19: The *in-situ* TEM observation on Ni#Y₂O₃.

Figure S20: HAXPES in the Ni 2*p* region for the Ni/Y₂O₃, Ni#Y₂O₃, and Ni/Al₂O₃.

Figure S21: HAXPES in the O 1*s* region.

Figure S22: HAXPES in the Y 3*d* region for the spent Ni/Y₂O₃- and Ni#Y₂O₃.

Figure S23: HAXPES in the Y 3*d* region for the fresh Ni-Y₂O₃ composites with different Ni/Y ratio.

Table S1: Physicochemical properties of the Ni-based catalysts.

Table S2: Catalyst amounts and the conversions for the TOF calculation.

Table S3: LT-DRM performance of different catalysts in a dense gas condition.

Table S4: The ratio of I_D/I_G for Ni/Al₂O₃, Ni/Y₂O₃ and Ni#Y₂O₃ after LT-DRM.

Supplementary Equations

References

Experimental Details

Catalyst preparation: Elemental Ni metal (The Nilaco Corporation) and Y metal (Rare Metallic Co., Ltd.) were melted at different atomic ratios using an arc torch in an Ar atmosphere (Ar purity: 99.9999%) to synthesize Ni-Y alloy precursors with different atomic ratios (Ni_5Y , Ni_3Y , Ni_2Y , NiY and NiY_3). The prepared Ni-Y alloy ingot was ground in a mortar and was sieved to obtain powder precursors with an average particle size of 50-60 μm . After the Ni-Y alloy precursors were heated in a gas stream consisting of CO , O_2 and Ar (Japan Fine Products Corporation; 2 vol% of CO , 1 vol% of O_2 and 97 vol % of Ar; gas flow rate: 60 mL min^{-1}) at 873 K for 12 hrs, we obtained the Ni- Y_2O_3 composites with different Ni/Y ratios. The Ni# Y_2O_3 catalyst was obtained from a NiY (Ni:Y=1:1) alloy precursor. Conventional supported catalysts of Ni/ Al_2O_3 and Ni/ Y_2O_3 were prepared as control by the impregnation method. An aliquot of 0.8 g of $\text{Ni}(\text{NO}_3)_2 \cdot 6\text{H}_2\text{O}$ (Sigma-Aldrich Co., Llc; 99.999%) was first dissolved in 20 mL of ethanol (Kishida Chemical Co., Ltd.; 99.5%). Then, 0.3 g of either Al_2O_3 or Y_2O_3 powder (Sigma-Aldrich Co., Llc.; nanopowder, <50 nm particle size) was added into the solution. The mixture was stirred for 8 hrs, and the ethanol solvent was removed by evaporation at 353 K to yield a green powder. The desired Ni/ Al_2O_3 and Ni/ Y_2O_3 catalysts were obtained after calcining the solid powder in a H_2 -Ar gas mixture (Japan Fine Products Corporation; 5 vol% of H_2 and 95 vol% of Ar) at 873 K for 4 hrs.

Characterization: The X-ray diffraction (XRD) patterns were recorded on an X-ray diffractometer (Panalytical X'Pert PRO) with Cu-K_α radiation. The surface morphologies of the samples were observed with a scanning electron microscope (SEM, Hitachi SU-8230, accelerating voltage: 10 kV). A focused ion beam (FIB, JEM-9320) was employed to section the sample. Transmission electron microscope (TEM) images were obtained with a JEOL 2100-F microscope with an operating voltage of 200 kV. Raman spectra were acquired with a Renishaw inVia 2000 Raman Microscope by using an Ar ion laser at a wavelength of 514.5 nm. Hard X-ray photoemission spectroscopy (HAXPES) was conducted by using an X-ray with a photon energy of 5.95 keV at the undulator beamline BL15XU of SPring-8, Japan. The

HAXPES spectra were acquired at room temperature under UHV using a hemispherical electron energy analyser (VG SCIENTA R4000). The binding energy was referenced to the Fermi edge of a Au thin film. H₂ pulse adsorption measurements were performed with a Micromeritics AutoChem II 2920 instrument. Aliquots of 0.1 g of the catalysts were first reduced in a H₂-Ar gas mixture (5 vol% H₂) at 673 K for 4 hrs prior to the H₂ adsorption. Pulses of H₂-Ar gas were introduced into the quartz reactor at 308 K. The total H₂ uptake was recorded until no further consumption of H₂ was recognized. H₂-O₂ titration was also performed with the Micromeritics AutoChem II 2920 instrument. An aliquot of 0.1 g of the sample was pretreated in a H₂-Ar gas mixture at 673 K for 4 hrs. Pulses of O₂-He (10 vol% O₂) gas were then introduced into the reactor. The consumption amount of O₂ was utilized to calculate the reduction degree by assuming the stoichiometric reoxidation of Ni⁰ to NiO. The Ni dispersion degree was calculated based on the number of exposed surface Ni atoms with respect to the total number of Ni atoms in the catalyst. In-situ TEM was performed with a JEM-1000K RS TEM (JEOL) at Nagoya University, which was equipped with a specially designed atmosphere-controllable cell. The sample was exposed to a reactant gas consisting of equimolar amounts of CH₄ and CO₂ at 200 Pa.

Catalytic tests: Low-temperature dry reforming of methane (LT-DRM) was performed on a fixed-bed flow reactor at atmospheric pressure. An aliquot of 0.1 g of the catalyst was loaded in a quartz reactor with an inner diameter of 10 mm. Then, a gas mixture of CH₄, CO₂ and Ar (CH₄:CO₂:Ar = 1:1:98 in vol%) at a flow rate of 100 mL min⁻¹ was introduced into the reactor. The temperature was raised to the desired reaction temperature, typically 723 K. The reaction effluents were analysed using a gas chromatograph equipped with an activated charcoal column. The catalytic performance over 6 hrs was typically used for the quantitative comparisons in the performance of different catalysts. The calculation methods for the consumption, formation and conversion rates are presented in the Supplementary Equations 1-7. The turn over frequency (TOF) was evaluated by using the same fixed-bed flow reactor. Both of the CH₄ and CO₂ conversion rates were always adjusted below 10 % by changing the catalyst weights. The TOF was finally calculated based on the conversion after the LT-

DRM reaction of 6 hrs.

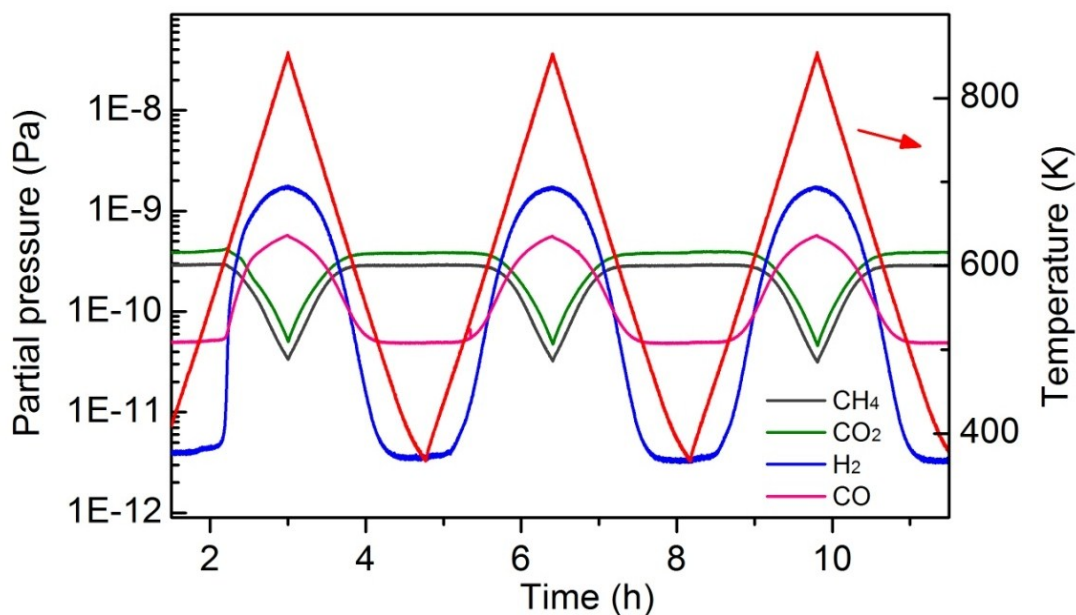


Figure S1. Low-temperature DRM over the Ni#Y₂O₃ catalyst at different temperatures. Temperature range: 373 K to 873 K. The sample was tested with a Micromeritics AutoChem II 2920 instrument. Note that the DRM reaction pathway ($\text{CH}_4 + \text{CO}_2 = 2\text{CO} + 2\text{H}_2$) was initiated at a low temperature of 623 K. The Ni#Y₂O₃ catalyst exhibited finite conversions of CH₄ and CO₂ as well as formation of CO and H₂ at higher temperatures than this onset temperature. Test conditions: catalyst amount = 0.1 g; CH₄/CO₂/Ar = 1/1/98 in vol %; total flow rate = 20 mL min⁻¹.

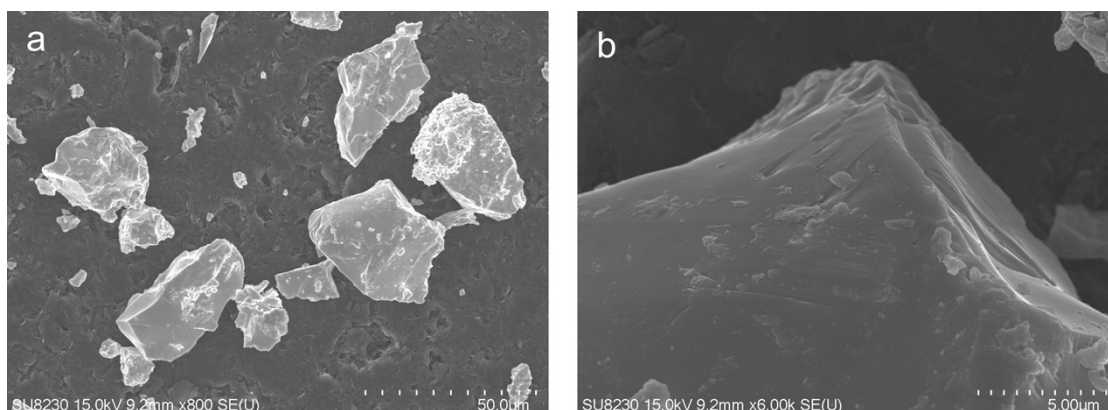


Figure S2. SEM images of the NiY (NiY = 1:1) alloy particles. (a) The particle morphology and (b) the outer surface.

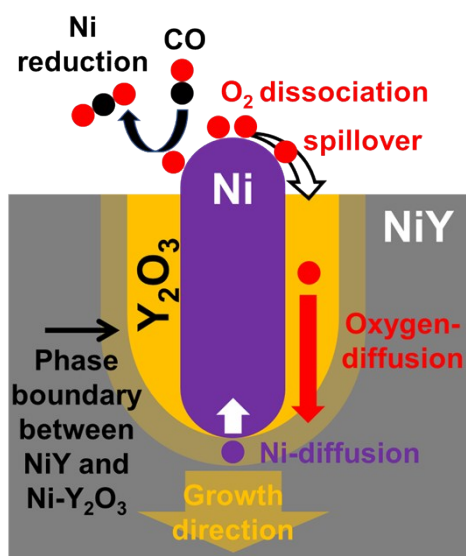


Figure S3. A possible mechanism for the nanophase separation occurring when the NiY alloy precursor is subjected at elevated temperatures to the atmosphere consisting of CO and O₂. The O₂ molecules are first absorbed on to the surface and dissociated to form atomic O. The atomic O further spills over the surface and disperses into the bulk to selectively oxidize NiY to Ni + Y₂O₃. The Ni phase is always retained as metal via reduction by CO. An entangled, fibrous network nanostructure spontaneously emerges out of the homogenous alloy precursor, following the unicursal track of the atomic diffusions. The size and dispersity of the nanostructure can be controlled by tuning the temperature and composition in the atmospheric processing (see Figure S7 and Figure 2 in the main text).

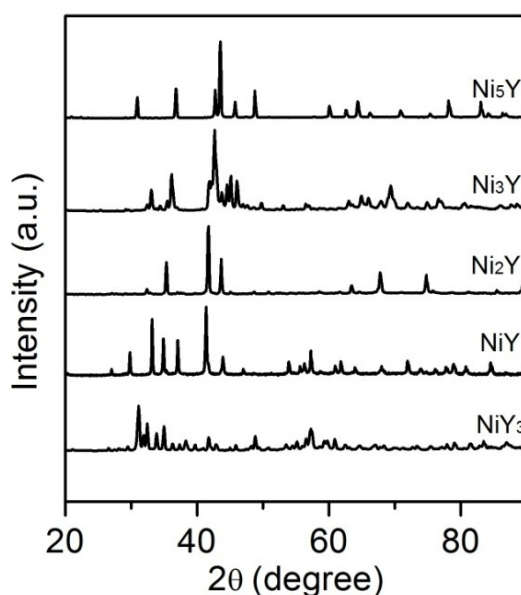


Figure S4. *p*XRD patterns for the alloy precursors of Ni₅Y, Ni₃Y, Ni₂Y, NiY and NiY₃.

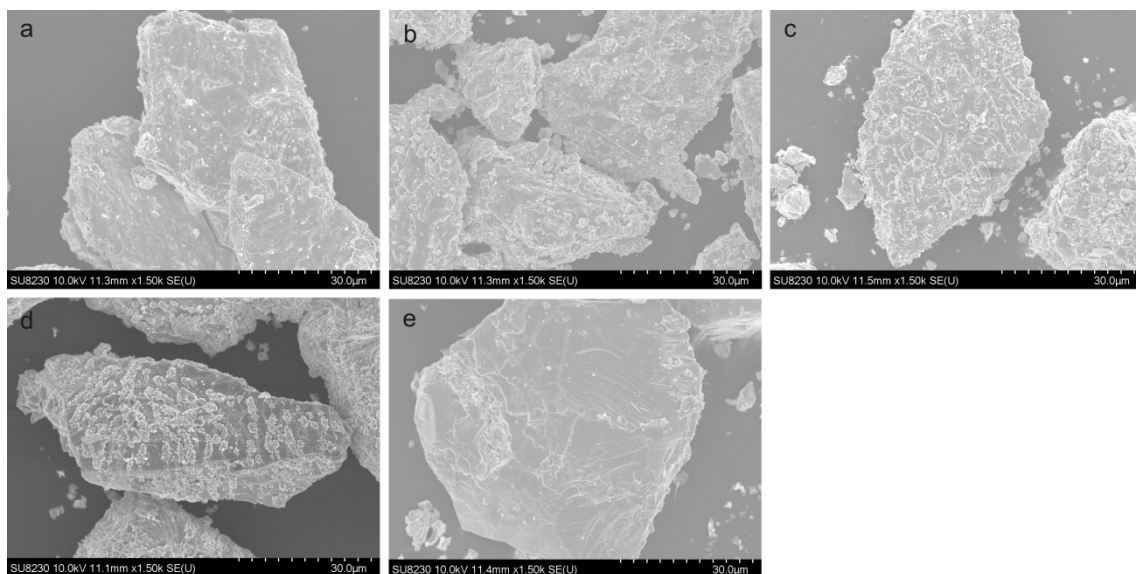


Figure S5. SEM images of the Ni-Y₂O₃ nanocomposites obtained from different Ni-Y alloy precursors with different Ni/Y ratios: (a) Ni/Y = 5/1, (b) Ni/Y = 3/1, (c) Ni/Y = 2/1, (d) Ni/Y = 1/1 and (e) Ni/Y = 1/3. The Ni-Y₂O₃ composite from an alloy precursor with Ni/Y = 1/1 corresponds to the Ni#Y₂O₃ catalyst. Note that there were a number of precipitates seen on the Ni/Y = 1/1 material, where the other materials had relatively smooth surfaces. As shown in Figure 3a, b in the main text, the Ni/Y=1/1 material corresponding to the Ni#Y₂O₃ catalyst exhibited the highest DRM activity among the other nanocomposites, which indicates that the precipitates on the surface plays the role of catalysis centre.

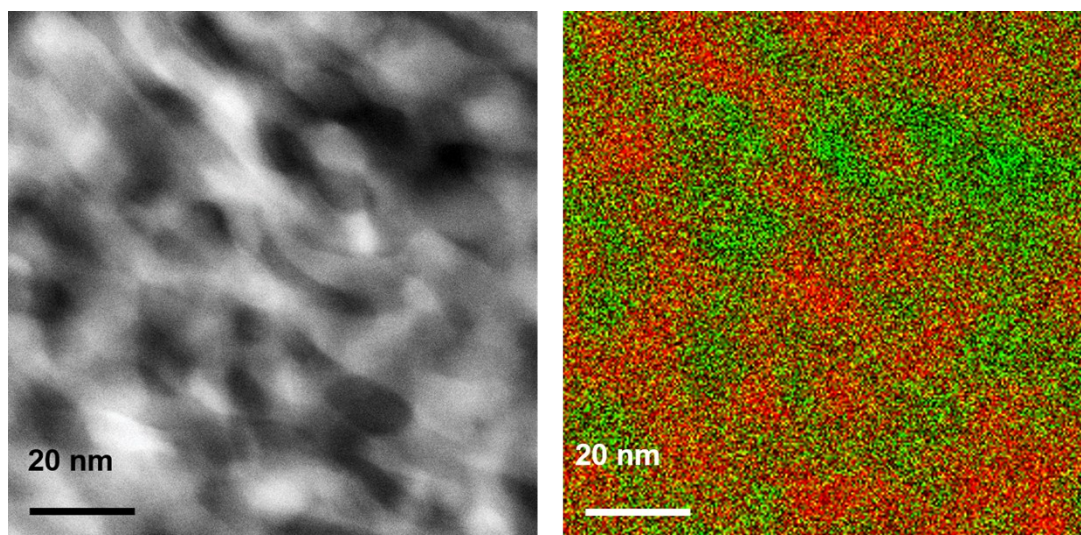


Figure S6. STEM images of the Ni#Y₂O₃ catalyst. STEM (*left*) and elemental mapping (*right*) of the Ni#Y₂O₃ section. These images were obtained with a JEM-ARM200F (JEOL) at an acceleration voltage of 200 kV.

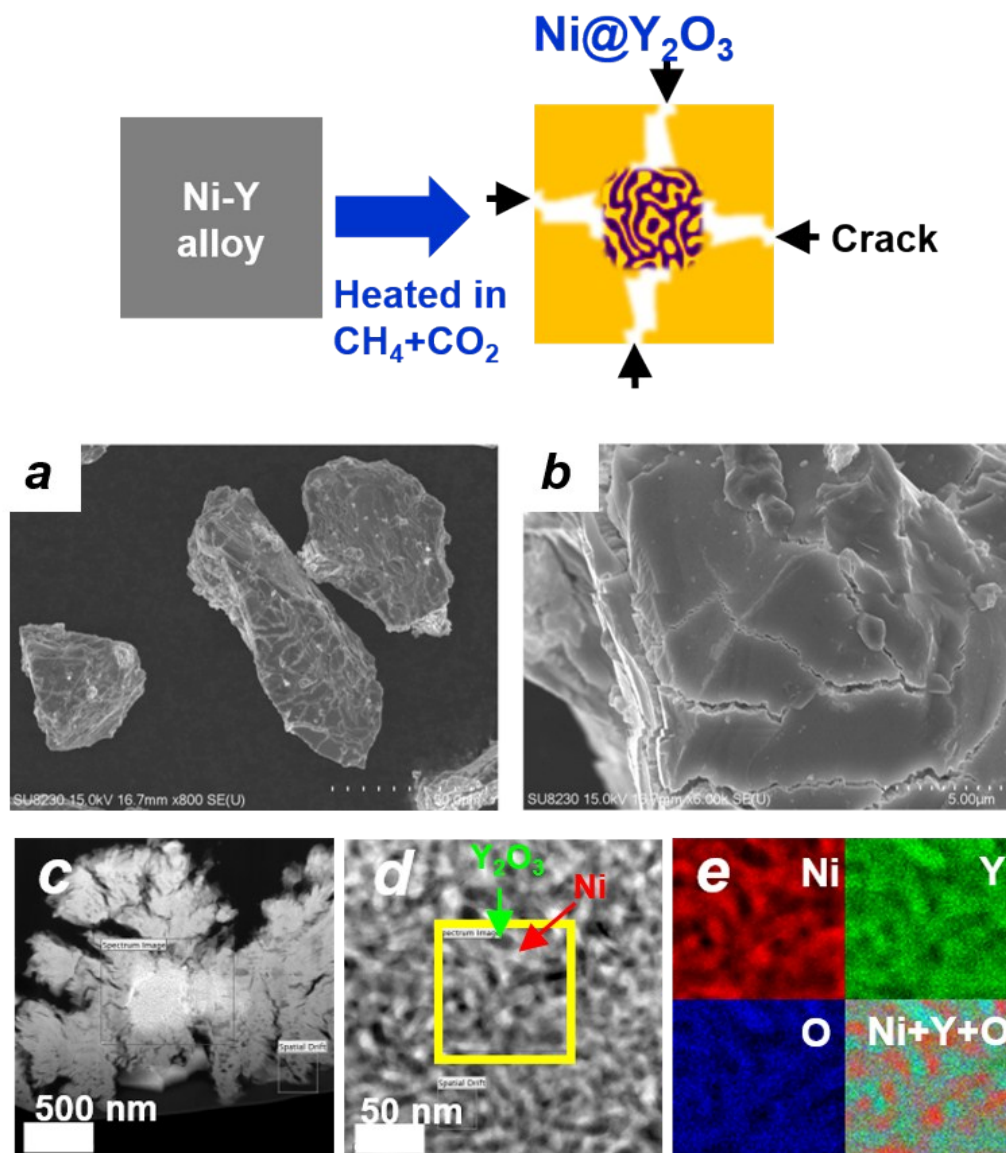


Figure S7. Atmospheric processing on the NiY precursor in CH_4/CO_2 ($\text{CH}_4:\text{CO}_2 = 1:1$ in volume %) yielded another Ni- Y_2O_3 composite with a significantly different microstructure from that of Ni# Y_2O_3 . The obtained material had a core-shell structure, (*i.e.*, Ni@ Y_2O_3), where the Ni-containing phase was encapsulated in a micrometre-thick Y_2O_3 shell. There were a number of cracks on the surface of the individual particles of Ni@ Y_2O_3 (a, b). The STEM observation on a sliced particle revealed that the cracks in the Ni@ Y_2O_3 particles propagated through the Y_2O_3 shell to reach a dense, high contrast core region (c). The high-magnification STEM and compositional mapping further showed that the fibrous metal Ni and Y_2O_3 phases were entangled with each other to form the core phase (d, e). Note that the high- and low-contrast regions in the STEM image corresponded to the Ni metal- and Y_2O_3 phases, respectively.

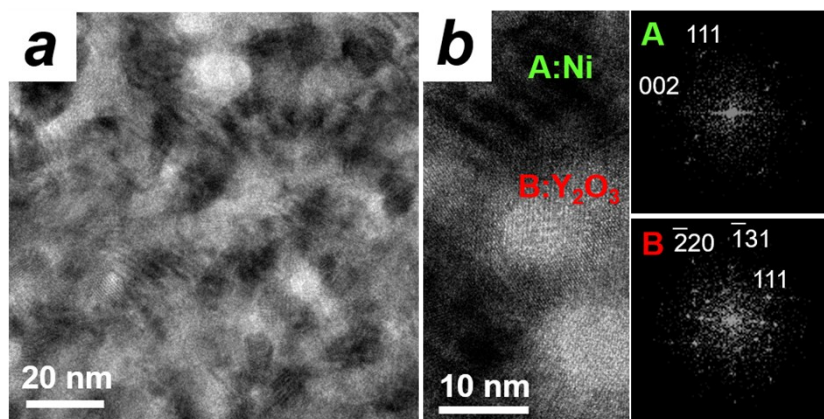


Figure S8. The lattice fringes for Ni#Y₂O₃ catalyst. (a) Section TEM image (JEM-ARM200F (JEOL) at an acceleration voltage of 200 kV) and (b) fast Fourier transform patterns from the A- and B-regions of (b), showing the A- and B-regions were consisted of Ni- and Y₂O₃, respectively (the indices in the insets correspond to the lattice fringes from Ni (A) and Y₂O₃ (B)).

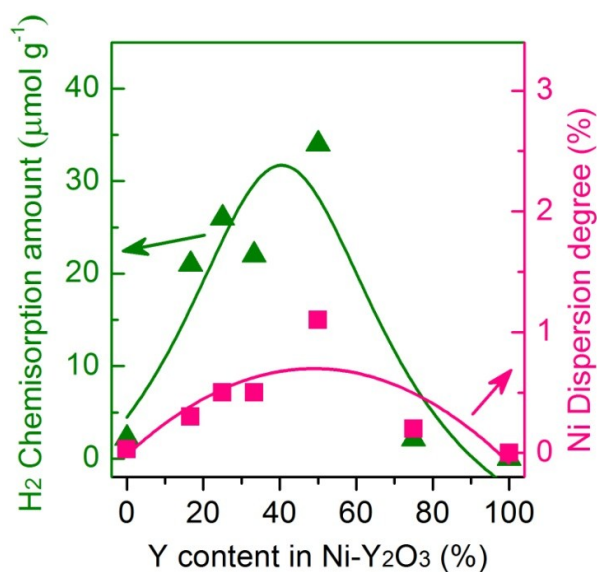


Figure S9. Influence of the Y content on H₂ chemisorption and Ni dispersion for Ni-Y₂O₃ composites.

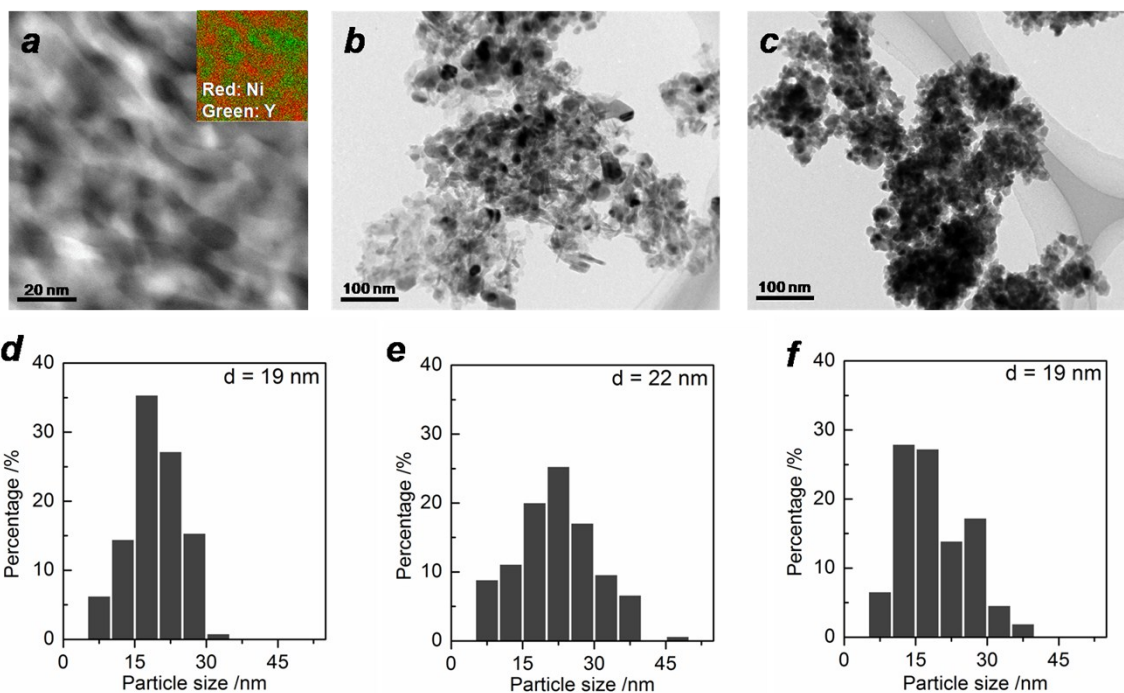


Figure S10. TEM observation and Ni particle size distribution for Ni#Y₂O₃, Ni/Al₂O₃, Ni/Y₂O₃. TEM observation: (a) Ni#Y₂O₃, (b) Ni/Al₂O₃, (c) Ni/Y₂O₃; Ni particle size distribution: (d) Ni#Y₂O₃, (e) Ni/Al₂O₃, (f) Ni/Y₂O₃. The mean Ni particle size was obtained by counting ca. 150 particles for each sample.

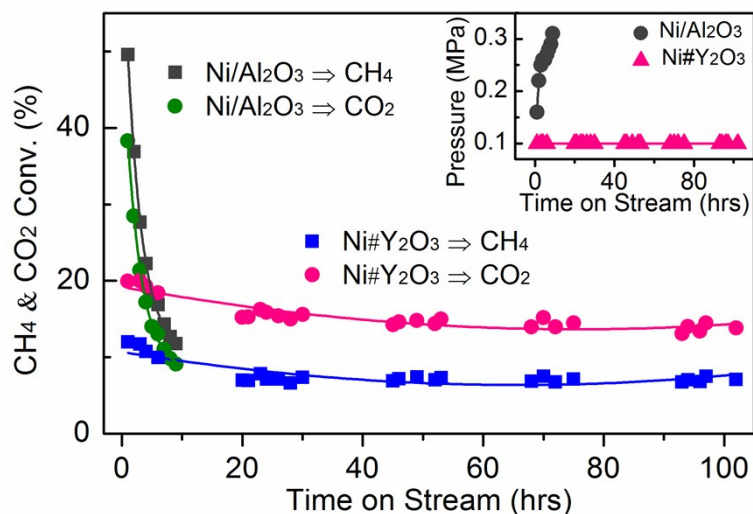


Figure S11. Stability of the Ni#Y₂O₃ in LT-DRM in a dense gas condition. Reaction conditions: Catalyst weight = 0.1g; Reactant gas mixture: CH₄/CO₂/N₂ = 10/10/5 mLmin⁻¹; Reaction temperature = 550 °C.

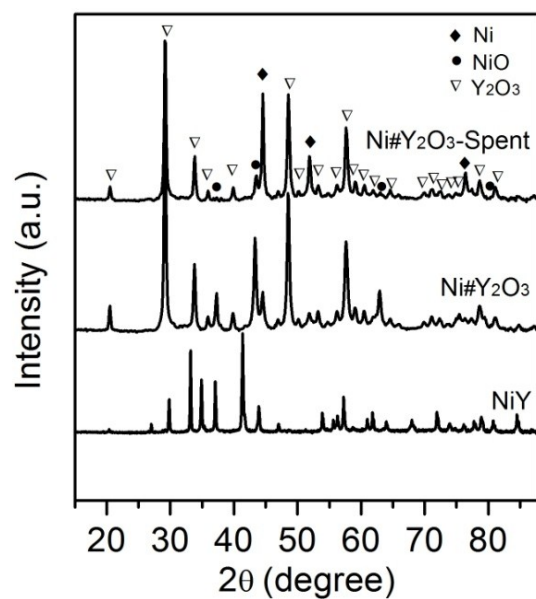


Figure S12. *p*XRD patterns for the NiY alloy precursor, fresh Ni#Y₂O₃ and a Ni#Y₂O₃ catalyst used for the LT-DRM for 6 hrs. As the result of a redox process of CO/O₂ gas, the most Y metal in NiY was converted into Y₂O₃, where the portion of Ni in NiY was converted into NiO and the other Ni was retained metallic. Compared with the fresh Ni#Y₂O₃, the spent Ni#Y₂O₃ catalyst contained more metallic Ni after LT-DRM reaction because the surface NiO was efficiently reduced back to the metallic Ni.

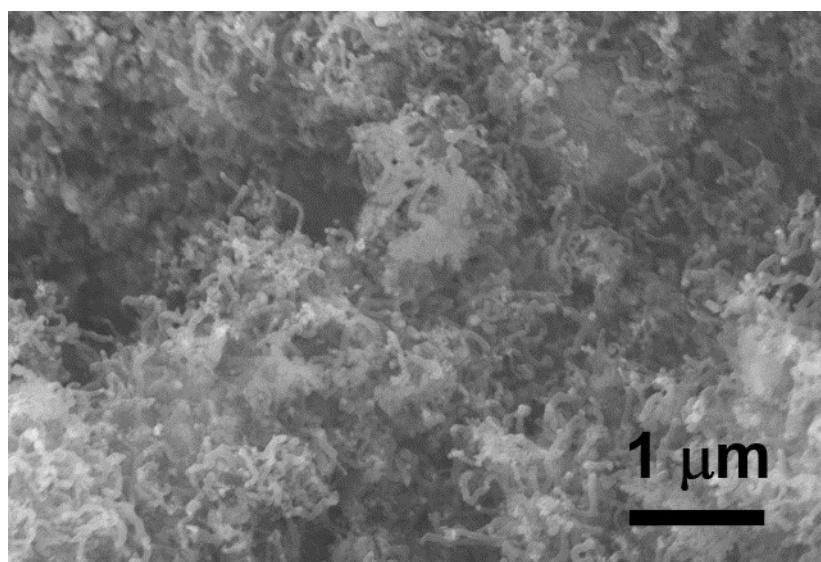


Figure S13. SEM image of a used Ni/Al₂O₃ catalyst.

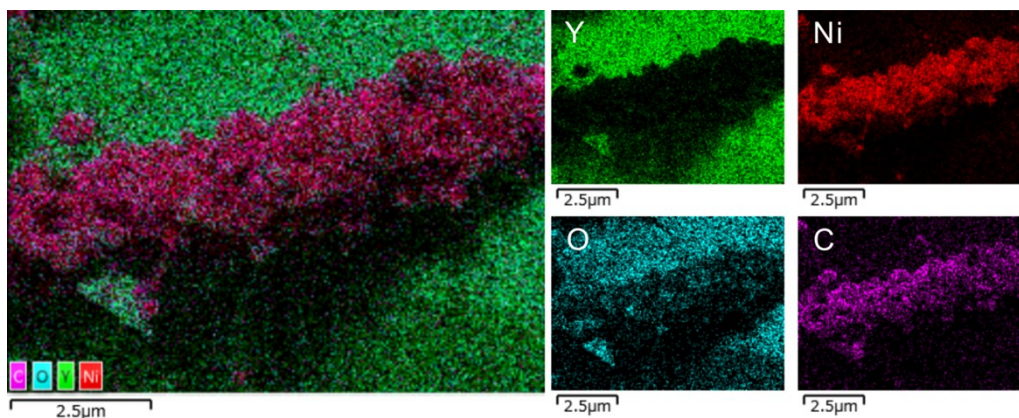


Figure S14. Compositional mapping images for the Ni#Y₂O₃ catalyst, 6 hrs after the exposure to LT-DRM.

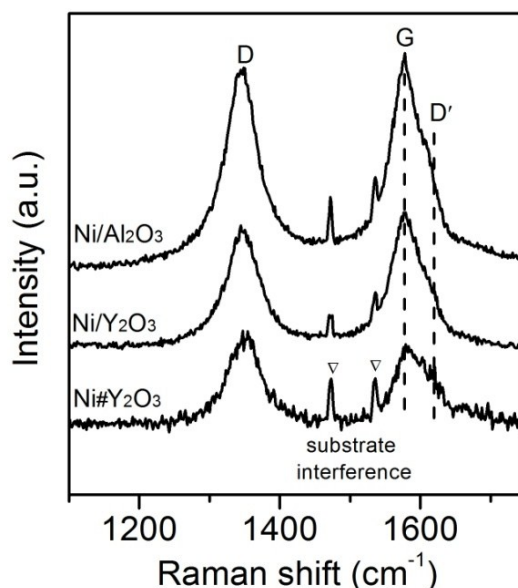


Figure S15. Raman spectra for Ni/Al₂O₃, Ni/Y₂O₃ and Ni#Y₂O₃ after LT-DRM. The G band is assigned to the first-order scattering of the E_{2g} mode of sp^2 carbon domains, arising from the C-C bond stretching of graphitic materials. The D band is assigned to a disordered structure of graphene.^[1,2] The D' band is ascribed to the randomly distributed impurities or surface charges in graphene. The sharp peaks at 1472 cm⁻¹ and 1536 cm⁻¹ were from the substrate. Compared to the traditional Ni/Al₂O₃ and Ni/Y₂O₃, Ni#Y₂O₃ showed enhanced D- and D' bands. The D band is more intense than the G band over Ni#Y₂O₃, whereas the G bands were more intense than the D bands over Ni/Al₂O₃ or Ni/Y₂O₃. Note that the relative intensity of the D' band to the G band is the most prominent over Ni#Y₂O₃ in comparison to any of the others. It was demonstrated that the used Ni#Y₂O₃ catalyst was more predominantly coated with disordered and/or impurity-containing graphene layers.

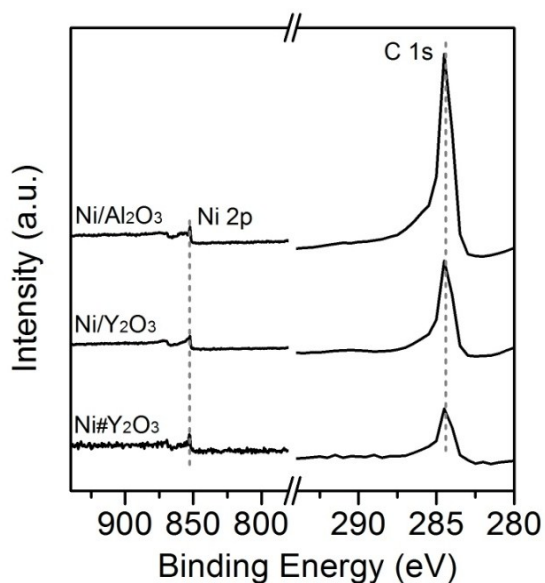


Figure S16. Hard X-ray photoemission spectra (HAXPES) in the Ni $2p$ - and C $1s$ regions for the different catalysts after LT-DRM. The C $1s$ photoemission intensities from the used catalysts increased in the following order: Ni#Y $_2$ O $_3$ < Ni/Y $_2$ O $_3$ < Ni/Al $_2$ O $_3$, while the Ni $2p$ intensity was the same. The Ni#Y $_2$ O $_3$ catalyst was less covered with carbon species than any of the other supported catalysts.

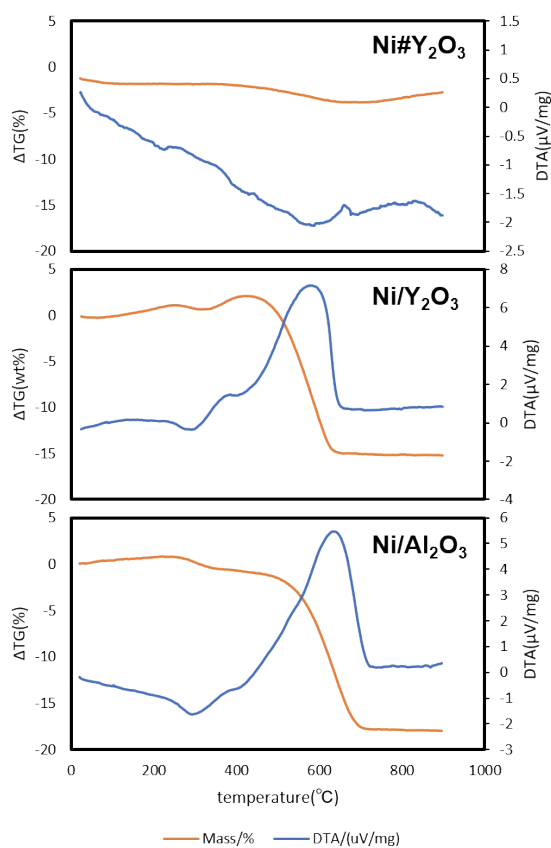


Figure S17. Thermo-gravimetry (TG) and differential temperature analysis (TDA) results for

Ni#Y₂O₃, Ni/Y₂O₃ and Ni/Al₂O₃, at elevating temperatures in an air stream. In advance to the TG/DTA experiments, each of the materials was first subjected to the diluted LT-DRM atmosphere (CH₄:CO₂:Ar=1:1:98; exposure for 12 hours) to promote carbon depositions.

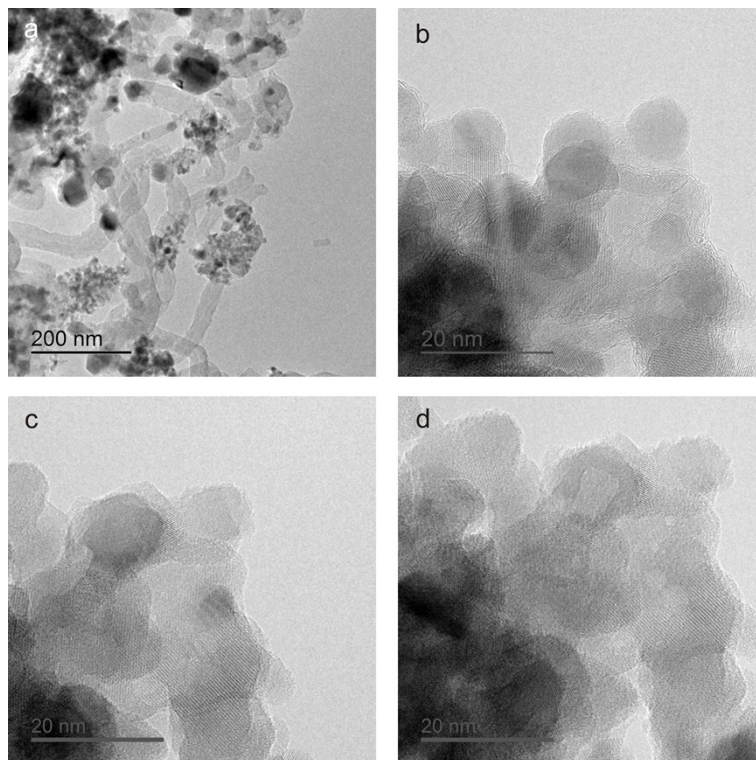


Figure S18. Conventional TEM- and *in-situ* TEM images for the Ni/Y₂O₃ catalyst. (a) The conventional TEM image for the Ni/Y₂O₃ catalyst 6 hrs after the exposure to the LT-DRM reaction. Reaction conditions: catalyst weight = 0.1 g; reaction temperature = 723 K; CH₄/CO₂/Ar = 1/1/98; flow rate = 100 mL min⁻¹. There were formed fibrous carbon deposits as over the Ni/Al₂O₃ catalyst (see Figure 4c in the main text). *In-situ* TEM images for the Ni#Y₂O₃ catalyst, (b)-(d): (b) 0.5 hrs, (c) 1.0 hrs; (d) 2.0 hrs after the exposure to a reactant gas of CH₄/CO₂ = 1/1 at 723 K with a pressure of 200 Pa.

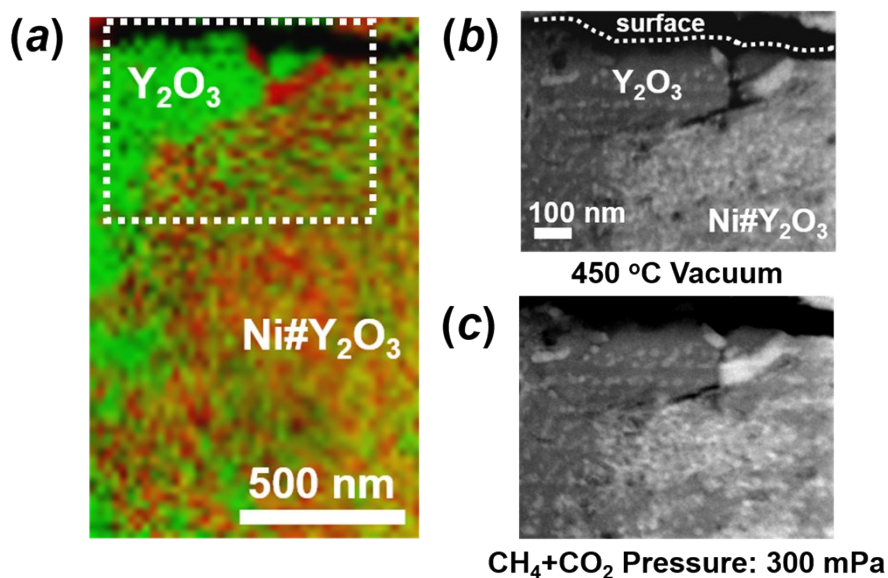


Figure S19. The *in-situ* TEM observation on Ni#Y₂O₃. (a) Compositional mapping image of a section of Ni#Y₂O₃, (b) *in-situ* annular-dark field (HAADF) STEM image before the DRM reaction, (c) the same section after the simulated DRM atmosphere of 6 hours.

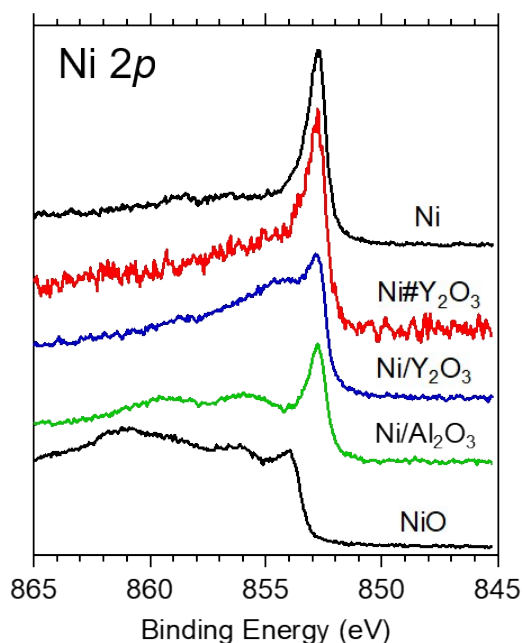


Figure S20. HAXPES in the Ni 2*p* region for the Ni/Y₂O₃, Ni#Y₂O₃, and Ni/Al₂O₃, after the use for LT-DRM at 723 K for 6 hrs. The HAXPES spectra for Ni- and NiO powders are presented as the reference. The Ni 2*p* spectrum for the Ni#Y₂O₃ was consisted of a single peak corresponding to metal Ni⁽⁰⁾ at a binding energy of 852.8 eV, whereas the Ni 2*p* spectra from Ni/Y₂O₃ and Ni/Al₂O₃ showed different satellite peaks at higher binding energy that correspond to cationic Ni of NiO and/or carburized Ni.

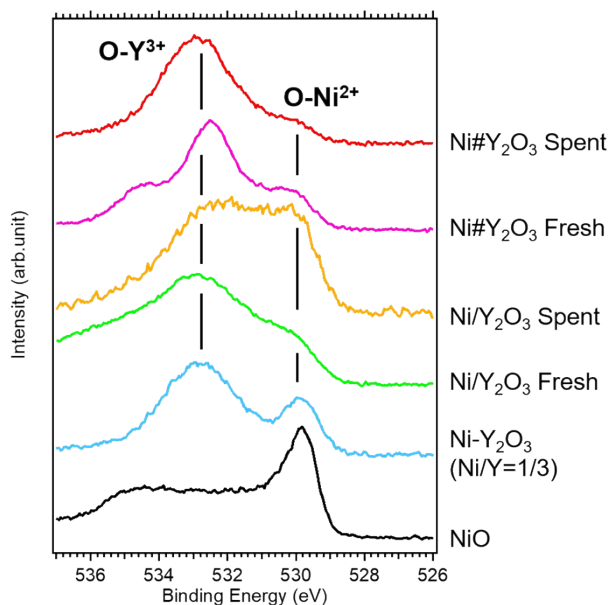


Figure S21. HAXPES in the O 1s region. The HAXPES results show that the as-prepared (Fresh) Ni/Y₂O₃ material mostly contained the Y-O bond, but after exposure to the DRM atmosphere, the O 1s emission from the Ni-O bond became more prominent (Ni/Y₂O₃ Spent), because of the oxidation of the Ni catalysis center. Unlike Ni/Y₂O₃, the O 1s emission from the Ni-O bond for Ni#Y₂O₃ was suppressed even after exposure to the DRM atmosphere. The HAXPES in the O1s region further showed that the Ni catalysis center of Ni#Y₂O₃ retained the metallic nature after exposure to the DRM atmosphere.

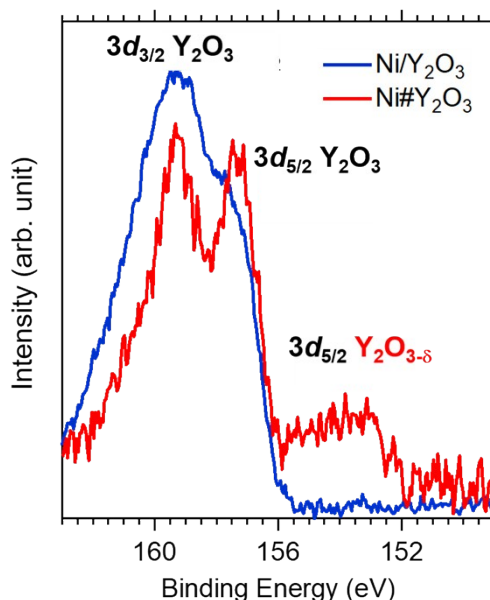


Figure S22. HAXPES in the Y 3d region for the spent Ni/Y₂O₃- and Ni#Y₂O₃ catalysts that were used for LT-DRM at 723 K for 6 hrs. The peaks at 157.3 eV and 159.3 eV respectively correspond to the Y 3d_{5/2}- and Y 3d_{3/2} emissions from filled Y₂O₃.^[3-5] Unlike the HAXPES spectra for Ni/Y₂O₃, there was observed a broad peak in the spectrum for Ni#Y₂O₃, ranging

from 156 to 152 eV. This broad peak is attributed to a Y $d_{5/2}$ emission from an oxygen-deficient yttrium oxide, *i.e.*, $Y_2O_{3-\delta}$ ($0 < \delta$), in which the Y atoms have lower apparent valence than +3 to establish the electric neutrality.

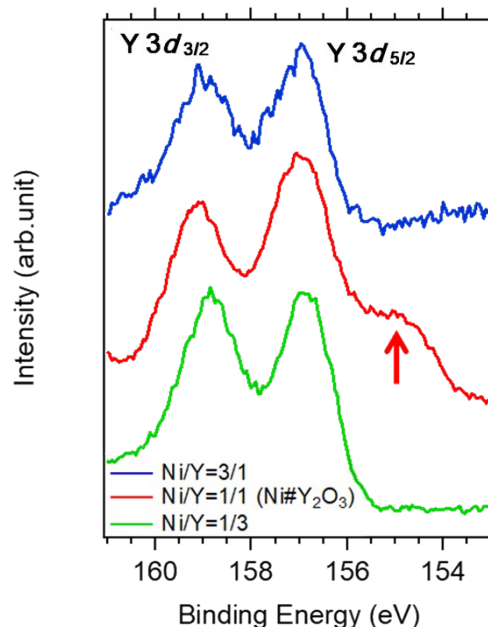


Figure S23. HAXPES in the Y 3d region for the fresh Ni-Y₂O₃ composites with different Ni/Y ratio. The catalysts with the ratio of 3/1 and 1/3 display similar peaks at 157.3 eV and 159.3 eV, which correspond to Y 3d_{5/2} and Y 3d_{3/2} of Y₂O₃, respectively. But, different with these two catalysts, the Ni#Y₂O₃ catalyst with the ratio of 1/1 shows more complex peak distributions. Moreover, a peak of low oxidation state of Y is observed from 156 to 154 eV. It indicate that the Ni#Y₂O₃ may be not completely oxidized in the calcination atmosphere, and the abundant oxygen vacancies are formed for the Y₂O₃ matrix. These oxygen vacancies can help to promote the CH₄ conversion. Thus, we obtain a higher TOF on the Ni#Y₂O₃. Oppositely, the overdose of Ni or Y for the catalysts with the ratio of 3/1 and 1/3 is not beneficial to form the oxygen vacancies.

Table S1. Physicochemical properties of the Ni-based catalysts.

Sample	Reduction degree ^a (%)	H ₂ chemisorption amount ^b ($\mu\text{mol g}^{-1}$)	Ni dispersion degree ^c (%)	Ni particle diameter ^e (nm)	Mean Ni size ^f (nm)	Mean Ni size ^g (nm)
Ni-powder	/	2.2	0.03 ^d	/	/	/
Ni#Y ₂ O ₃	25	34	4.5	21	19	20
Ni/Al ₂ O ₃	63	74	3.9	24	22	25
Ni/Y ₂ O ₃	69	101	4.9	20	19	22

(a) Evaluated by H₂-O₂ titration; (b) measured by the H₂-pulse method. (c) calculated from the H₂ chemisorption amount; (d) Ni dispersion on the Ni powder was calculated based on the number of exposed surface Ni atoms with respect to the total number of Ni atoms in the catalyst. (e) calculated using the following equation: Ni diameter = 0.971/dispersion;^[6,7] (f) evaluated from the TEM images for the fresh catalysts; (g) evaluated from the TEM images for spent catalysts.

Table S2. Catalyst amounts and the conversions for the TOF calculation.

Sample	Amount of catalyst used (mg)	CH ₄ Conv. (%)	TOF _{CH₄} [10^{-2} s^{-1}]
Ni-powder	100	0.4	0.7
Ni-Y ₂ O ₃ (Ni/Y=5/1)	25	2.7	1.9
Ni-Y ₂ O ₃ (Ni/Y=3/1)	27	2.9	1.5
Ni-Y ₂ O ₃ (Ni/Y=2/1)	25	1.6	1.1
Ni#Y ₂ O ₃ (Ni/Y=1/1)	7.0	3.0	4.7
Ni-Y ₂ O ₃ (Ni/Y=1/3)	100	0.7	1.2
Y ₂ O ₃	/	/	/
Ni/Al ₂ O ₃	1.1	5.9	27
Ni/Y ₂ O ₃	1.2	4.9	15

Reaction conditions: reaction temperature = 723 K; CH₄/CO₂/Ar = 1/1/98; flow rate = 100 mL min⁻¹. The conversions were quantified at a time course of 6 hrs after exposed to the reaction atmosphere.

Table S3. LT-DRM performance of different catalysts in a dense gas condition.

Sample	CH ₄ Consumption Rate [mmol h ⁻¹]	CO ₂ Consumption Rate [mmol h ⁻¹]	H ₂ Formation Rate [mmol h ⁻¹]	CO Formation Rate [mmol h ⁻¹]	Carbon balance
Ni/Al ₂ O ₃	15	10	18	7.7	3.2
Ni/MgO	9.1	8.7	14	12	1.3
Ni#Y ₂ O ₃	3.1	4.8	4.5	7.8	1.0

Reaction conditions: Catalyst weight = 0.1g; Reactant gas mixture: CH₄/CO₂/N₂ = 10/10/5 mLmin⁻¹; Reaction temperature = 550 °C. An aliquot of 6 hr after the exposure to the reactant gas mixture. N₂ gas of a known flux (5 mL min⁻¹) was used as an inner standard to quantify the fluxes of each of the gas species. The carbon balance was calculated as $([\text{CH}_4 \text{ consumption rate}] + [\text{CO}_2 \text{ consumption rate}]) / [\text{CO formation rate}]$. Note that magnesia-supported Ni (Ni/MgO), as well as Ni/Al₂O₃, showed a larger carbon balance than unity, although Ni/MgO is acknowledged to be most carbon-deposition tolerant among all the known Ni-based catalysts. Unlike any of the supported catalysts, Ni#Y₂O₃ established the unity of carbon balance, where the summation of CH₄- and CO₂ consumption rates (7.9 mmol h⁻¹) was coincident with the CO formation rate (7.8 mmol h⁻¹) within experimental errors.

Table S4. The ratio of I_D/I_G for Ni/Al₂O₃, Ni/Y₂O₃ and Ni#Y₂O₃ after LT-DRM.

Sample	I _D /I _G
Ni/Al ₂ O ₃	0.9
Ni/Y ₂ O ₃	0.9
Ni#Y ₂ O ₃	1.2

The ratio of I_D/I_G for the D band and G band was calculated from the integrated intensity of the peaks. The conventional catalysts of Ni/Al₂O₃ and Ni/Y₂O₃ uncover same I_D/I_G ratio, but the Ni#Y₂O₃ possesses a higher ratio than the conventional catalysts. The higher ratio of I_D/I_G suggests that the more disordered and deficient carbon species over the Ni#Y₂O₃ is formed. They are more beneficial to be oxidized than the CNT or graphitic carbon.

Supplementary Equations: Calculation details for the LT-DRM performance.

$$(1) \text{ CH}_4 \text{ Conv. [\%]} = \frac{\text{mol of CH}_4 \text{ input} - \text{mol of CH}_4 \text{ output}}{\text{mol of CH}_4 \text{ input}} \times 100$$

$$(2) \text{ CO}_2 \text{ Conv. [\%]} = \frac{\text{mol of CO}_2 \text{ input} - \text{mol of CO}_2 \text{ output}}{\text{mol of CO}_2 \text{ input}} \times 100$$

$$(3) \text{ CH}_4 \text{ Consumption Rate} = \text{flow rate of CH}_4 \text{ input} \times \text{CH}_4 \text{ Conv.}$$

$$(4) \text{ CO}_2 \text{ Consumption Rate} = \text{flow rate of CO}_2 \text{ input} \times \text{CO}_2 \text{ Conv.}$$

$$(5) \text{ H}_2 \text{ Formation Rate} = \text{flow rate of CH}_4 \text{ input} \times \frac{\text{mol of H}_2 \text{ output}}{\text{mol of CH}_4 \text{ input}}$$

$$(6) \text{ CO Formation Rate} = (\text{flow rate of CH}_4 \text{ input} + \text{flow rate of CO}_2 \text{ input})$$

$$\times \frac{\text{mol of CO output}}{(\text{mol of CH}_4 \text{ input} + \text{mol of CO}_2 \text{ input})}$$

$$(7) \text{ H}_2/\text{CO ratio} = \frac{\text{H}_2 \text{ Formation Rate}}{\text{CO Formation Rate}}$$

References

1. A. C. Ferrari, J. Robertson, *Phys. Rev. B*, 2000, **61**, 14095-14107.
2. M. A. Pimenta, G. Dresselhaus, M. S. Dresselhaus, L. G. Cancado, A. Jorio, R. Saito, *Phys. Chem. Chem. Phys.*, 2007, **9**, 1276-1290.
3. X. Huang, G. Xue, C. Wang, N. Zhao, N. Sun, W. Wei, Y. Sun, *Catal. Sci. Technol.*, 2016, **6**, 449-459.
4. G. B. Sun, K. Hidajat, X. S. Wu, S. Kawi, *Appl. Catal. B*, 2008, **81**, 303-312.
5. P. Malacrida, H. G. S. Casalongue, F. Masini, S. Kaya, P. Hernández-Fernández, D. Deiana, H. Ogasawara, I. E. L. Stephens, A. Nilsson, I. Chorkendorff, *Phys. Chem. Chem. Phys.*, 2015, **17**, 28121-28128.
6. C. H. Bartholomew, R. J. Farrauto, *J. Catal.*, 1976, **45**, 41-53.
7. C. H. Bartholomew, R. B. Pannell, *J. Catal.*, 1980, **65**, 390-401.